Tailoring MnO₂ Cathode Interface via Organic-Inorganic Hybridization Engineering for Ultra-Stable Aqueous Zinc-Ion Batteries

Yaxi Ding, Chun Cai, Longtao Ma, Jiahong Wang, Michael Peter Mercer, Jun Liu, Denis Kramer, Xuefeng Yu, Dongfeng Xue*, Chunyi Zhi*, Chao Peng*

Y. X. Ding, C. Cai, Dr. J. H. Wang, Prof. X. F. Yu, Dr. C. Peng
Materials Interfaces Center, Shenzhen Institute of Advanced Technology, Chinese Academy of Sciences
Shenzhen 518055, Guangdong, China
E-mail: chao.peng@siat.ac.cn

Prof. C. Y. Zhi
Department of Materials Science and Engineering, City University of Hong Kong
Kowloon, Hong Kong 999077, China
E-mail: chunyzhi@cityu.edu.hk

Prof. D. F. Xue
Shenzhen Institute for Advanced Study, University of Electronic Science and Technology of China
Shenzhen 518110, China
E-mail: dfxue@uestc.edu.cn

Prof. L. T. Ma, Prof. J. Liu
School of Materials Science and Engineering, Guangdong Provincial Key Laboratory of Advanced Energy Storage Materials, South China University of Technology
Guangzhou 510641, China

Dr. M. P. Mercer, Prof. D. Kramer
Helmut-Schmidt-University, University of the Armed Forces
Hamburg 22043, Germany

1

Abstract

Manganese (Mn)-based aqueous zinc ion batteries show great promise for large-scale energy storage due to their high capacity, environmental friendliness and low cost. However, they suffer from the severe capacity decay associated with the dissolution of Mn from the cathode/electrolyte interface. In this study, our theoretical modeling inspires that the amino acid molecule, isoleucine (Ile), can be an ideal surface coating material for α-MnO$_2$ to stabilize the surface Mn lattice and mitigate Mn dissolution, thereby enhancing cycling stability. Furthermore, the coated Ile molecular layers can accumulate Zn^{2+} ions from the electrolyte and promote those ions' transport to the α-MnO$_2$ cathode while prohibiting H$_2$O accessing the α-MnO$_2$ surface, reducing the surface erosion. We experimentally synthesized the compact organic-inorganic interface for α-MnO$_2$ utilizing Ile that shows homogeneous distribution on the well-defined Ile-α-MnO$_2$ nanorod electrodes. The fabricated aqueous zinc-ion battery exhibits a high specific capacity (332.8 mAh/g at 0.1 A/g) and excellent cycling stability (85% after 2000 cycles at 1 A/g) as well as good inhibition towards Mn^{2+} dissolution, surpassing most reported cathode materials. This organic-inorganic hybrid interface design provides a new, simple avenue for developing high-performance and low-cost Mn-based aqueous zinc ion batteries.

1. Introduction

The large-scale renewable energy storage is attracting great attention due to the rapid pace of clean energy development. The demand for high-performance electrochemical batteries is growing fast, and the requirements are becoming more and more stringent, which must be safe, environmentally friendly, cost-effective and have a long cycle/calendar life.[1,2] Lithium-ion batteries (LIBs) are widely commercialized energy-storage batteries for their long life and high energy density. Their flammable and toxic organic electrolyte, however, poses a potential safety risk for their further development.[3] In contrast, aqueous zinc ion batteries (AZIBs) present a promising avenue for next-generation large-scale energy storage owing to their high theoretical specific capacity (820 mAh/g), low redox potential (-0.76 V vs. SHE), and most importantly, the inherent safety of utilizing the aqueous electrolyte, which effectively prevents fire risks.[4] Although these attractive properties are commendable, AZIBs still face severe difficulties due to the limited choices of cathode materials to achieve long-term cycling and high energy density. There has been considerable attention being directed towards cathode materials, such as V-based, Mn-based inorganics, Prussian blue analogs, and organic compounds,[5,6] aiming to identify cost-effective and reliable electrode candidates with extended lifespans and high-rate capabilities. Among those, manganese dioxide (MnO_2) has emerged as one of the promising cathode materials for AZIBs and has attracted wide studies due to its environmental friendliness, low cost, and high voltage plateau.[7]

However, MnO_2 cathodes still face several challenges, such as cycling stability, low electronic conductivity and reactivity, which are far from satisfactory.[8] The Jahn-Teller distortion and high lattice strain induced by the inserted Zn^{2+} in the MnO_2 cathode structure as well as the low diffusion coefficient of Zn^{2+}, further lead to poor structural stability and slow reaction kinetics.[9] During cycling, MnO_2 cathodes also suffer from a non-negligible problem of dissolution of the active substance. In addition, the formation of irreversible phases (e.g.,

from α-, β-, or γ- phases to layered structures) can easily lead to subsequent structural collapse or electrode crushing, resulting in poor cycling stability.[10,11] Adding $MnSO_4$ to the electrolyte (to balance the dissolution of Mn^{2+}) effectively slows the dissolution of the cathode.[12,13] However, it cannot fundamentally address the dissolution problem of Mn-based cathodes. Besides, introducing metal ions into the manganese oxide layer/tunnel can inhibit manganese dissolution by forming manganese-oxygen bonding to form manganese polyhedral.[14-16] Nevertheless, many pre-embedded cations in MnO_2 may experience electrostatic repulsion between the pre-embedded cations and the inserted carrier ions, hindering ionic diffusion. In some cases, the pre-embedded cations/molecules may be extracted from the MnO_2 cathode into the electrolyte during cycling, thus losing the desired effect of inhibiting manganese dissolution and stabilizing the structure.[17] Therefore, exploring effective strategies to improve structural stability, electrochemical reactivity, and cycle life of MnO_2 cathodes in Zn-MnO_2 batteries is still challenging.

Interface engineering is an effective strategy to improve the electrochemical properties of electrode materials, which can be used to suppress interfacial side reactions, increase specific surface area, and improve conductivity. Among them, the organic-inorganic hybrid strategy attracts widespread attention. The inorganic materials contribute high electrical conductivity and well-ordered morphology for rapid ion transport. At the same time, the organic part can isolate the electrolyte from the cathode to mitigate the side reactions and inhibit the dissolution of metal oxides.[18-20] Amino acids, containing the elements C, H, N, and O, are the most common organic compounds and can be easily obtained from natural or commercial raw materials at low cost. The amino acids are characterized by electron-rich functional groups of -NH_2, which easily bind with the electrode to form the stable, compact molecular layers coating on the electrode surface.[21-25]

In this study, the goal is to identify a suitable amino acid molecule that can be coated on an α-MnO_2 cathode as molecular layers to mitigate the dissolution of Mn and the erosion of α-

4

MnO_2 cathode by combining density functional theory (DFT) calculations and experiments. DFT calculations indicate the isoleucine (Ile) molecules are thermodynamically stable when adsorbed at Mn sites on the α-MnO_2 surface via Mn-N bond formation and form uniform molecular layers that stabilize lattice-Mn sites. Furthermore, it acts as a catcher to accumulate Zn^{2+} from the electrolyte and promotes their transport into the α-MnO_2 cathode while is unfavorable for H_2O molecules diffusing into α-MnO_2. Inspired by this theoretical prediction, we attempted to explore the organic-inorganic hybridization strategy to synthesize the isoleucine-coated α-MnO_2 (Ile-α-MnO_2) and adopt it for AZIBs. The Ile-α-MnO_2 electrode material exhibited a high reversible specific capacity of 332.8 mAh/g at a current density of 0.1 A/g, and maintained 85% of the initial capacity at a current density of 1 A/g after 2000 cycles. This strategy not only breaks the compromise between fast kinetics and high stability of conventional anode materials but also provides new ideas for designing advanced energy storage materials.

2. Results and Discussion
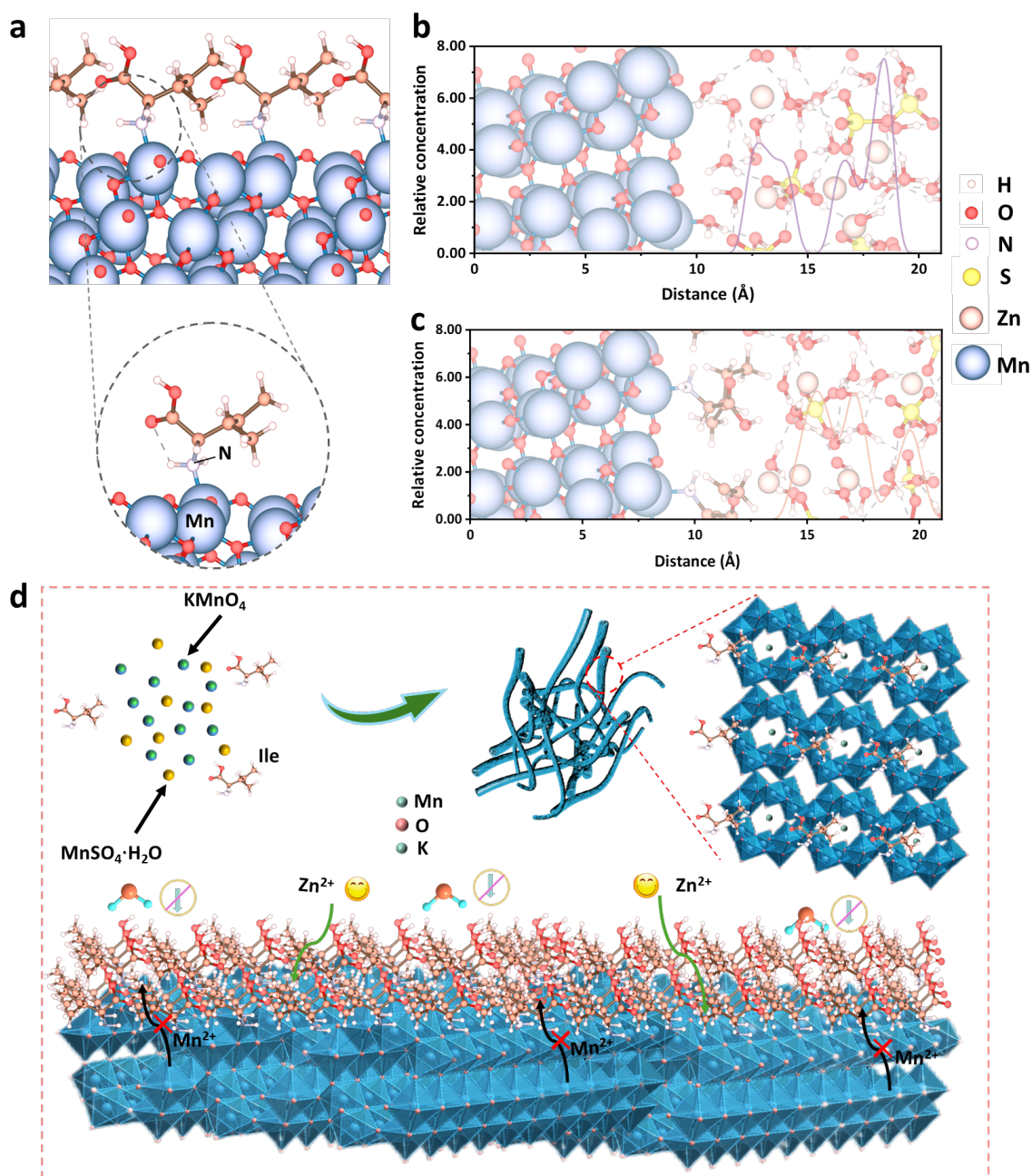
Figure 1. The organic-inorganic hybridization interface on the α-MnO$_2$ (211) surface and Zn^{2+} concentration profiles as well as the schematic synthesis of Ile-α-MnO$_2$. (a) shows the Ile adsorption and coating on α-MnO$_2$(211) surface via formed Mn-N bonds. (b) and (c) are the relative concentrations of Zn^{2+} in aqueous electrolyte along Z axis of bare α-MnO$_2$(211) and Ile-α-MnO$_2$(211), respectively. (d) Schematic diagram showing the interface engineering of α-MnO$_2$ nanorods utilizing the organic isoleucine molecules.

Five types of amino acid molecules, namely isoleucine, cysteine, arginine, serine, methionine, were investigated (Figure S1). DFT calculations indicate that the isoleucine (Ile) molecule shows attraction towards Zn^{2+} and the best hydrophobicity among those molecules. Hence, the Ile was selected as the model to verify our hypothesis that organic-inorganic hybridization interface forms on the α-MnO_2(211) surface.[26,27] As illustrated in Figure 1a, the Ile molecules can steadily adsorption on α-MnO_2(211) surface with the N atom binding at the Mn site with an adsorption energy of -1.45 eV, indicating the strong chemical adsorption of Ile. The adsorption energy only changes slightly to -1.48 eV when Ile molecules reach full coverage on the α-MnO_2(211) surface, which demonstrates Ile molecules can be stably coated as a layer outside the α-MnO_2. *Ab-inito* molecular dynamics (AIMD) are performed afterward to understand the interactions of Ile molecular layer at the α-MnO_2(211)/electrolyte interface. In a bare α-MnO_2(211)/electrolyte system, the relative concentration of Zn^{2+} ions is averagely distributed in the aqueous electrolyte (Figure 1b and S2). In contrast, there is a higher Zn^{2+} concentration close to the Ile molecular layer than in the bulk electrolyte (Figure 1c), implying the Ile molecules can promote the accumulation of Zn^{2+} at the Ile/electrolyte interface and might enhance Zn^{2+} intercalation.

Relying on the theoretical concept, we prepared the isoleucine-coated MnO_2 nanorods, as shown in Figure 1d. Briefly, Ile-α-MnO_2 was prepared by a simple one-step hydrothermal method in a mixed solution and a small amount of hydrochloric acid was added to adjust the pH of Ile. The phase structure of the sample was characterized by X-ray diffraction (XRD). As shown in Figure 2a, all the diffraction peaks corresponded to the [2 × 2] tunneling structure of α-MnO_2 (JCPDS No. 44-0141) with no other impurities, indicating the high purity of the crystalline phase.[28] The peak intensity of Ile-α-MnO_2 is relatively weak due to the organic Ile coating, suggesting that the particle size is reduced and more homogeneous after the formation of the hybridized structure compared to the pristine α-MnO_2. The Raman spectroscopy was characterized to elucidate further the interaction between the coated Ile and α-MnO_2 substrate.

The low-frequency Raman bands near 574 and 641 cm^{-1} can be attributed to the stretch-symmetric Mn-O oscillations of the [MnO$_6$] group.[29] Compared with pristine manganese dioxide, the peaks of Mn-O bonds in Ile-α-MnO$_2$ (Figure S3) show a blue-shift due to the coating of Ile. According to the Hooke's law (Eq. (1)), the bonding force constant (k) of α-MnO$_2$ can be used to estimate the bonding strength, and k is positively correlated with ω^2. After introducing Ile organic layers, the Raman becomes blue-shifted and k value decreases. Hence, the Mn-O bond becomes weaker, and the binding energy of Mn-O bond reduces, which might induce the formation of oxygen vacancies.[30-32] Furthermore, Ile-α-MnO$_2$ exhibits attenuated C-N$^+$ stretching vibrations and low-wave-number displacements of the characteristic peaks, suggesting that a chemical bond (Mn-N) has been formed between α-MnO$_2$ and Ile.[33] This highly agrees with our theoretical analysis. Figure S4 illustrates the theoretical charge density difference of Ile-α-MnO$_2$ that there is a multitude of electron densities transferring from the α-MnO$_2$(211) slab to the Ile molecules due to the generated electrostatic potential gradient at the interface. The crystal orbital Hamilton population (COHP) analysis also indicates there are considerable bonding states below the Fermi level contributed by the N $2p$ and Mn $3d$ orbital interactions.

$$\omega = \frac{1}{2\pi c} \sqrt{k/\mu} \tag{1}$$

X-ray photoelectron spectroscopy (XPS) was used to characterize the chemical composition and defects of Ile-α-MnO$_2$ nanorods. In contrast to the α-MnO$_2$ nanorods (Figure S5), the XPS measurement spectra of Ile-α-MnO$_2$ show the component consisting of N, Mn, O and K elements. Furthermore, the Mn $2p$ peak of Ile-α-MnO$_2$ (642.3 eV for Mn $2p_{3/2}$ and 654.0 eV for Mn $2p_{1/2}$) is shifted to a higher position as compared to α-MnO$_2$ (642.2 eV for Mn $2p_{3/2}$ and 654.0 eV for Mn $2p_{1/2}$), indicating that there is higher valence state of Mn in Ile-α-MnO$_2$ during the electrochemical oxidization process (Figure S6).[34] In the N $1s$ spectrum, two characteristic peaks occur at 400.1 and 398.8 eV (Figure 2b), where the peak at 400.1 eV

belongs to the Mn-N bonding.[35] Meanwhile, the O 1s XPS patterns show peaks located at 531.2 and 529.7 eV in both the Ile-α-MnO$_2$ and the α-MnO$_2$, which correspond to the Mn-O bonds and oxygen vacancy defects, respectively.[36] It is noteworthy that the peak intensities
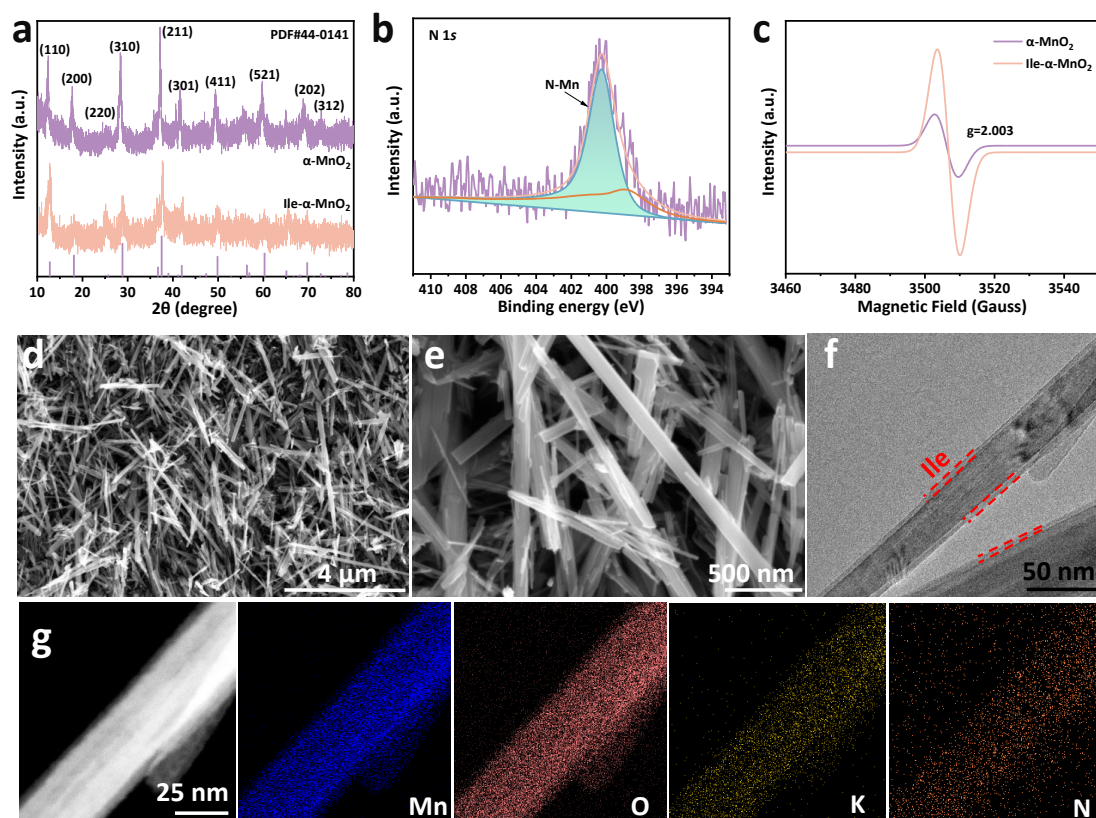
Figure 2. Structural characterization analysis. (a) XRD patterns of α-MnO$_2$ and Ile-α-MnO$_2$. (b) N 1s XPS spectra. (c) EPR spectra of α-MnO$_2$ and Ile-α-MnO$_2$. (d)~(e) are the SEM images of Ile-α-MnO$_2$. (f) HRTEM of the as-prepared Ile-α-MnO$_2$. (g) Elemental mapping images of Ile-α-MnO$_2$ nanorods.

of the oxygen defects in Ile-α-MnO$_2$ are much higher than those in α-MnO$_2$, which reflects the higher concentration of oxygen defects in Ile-α-MnO$_2$ (Figure S7). As shown in Figure 2c, the symmetric peak of Ile-α-MnO$_2$ shows a stronger signal intensity at a typical g factor of 2.003 than that of α-MnO$_2$, which originates from the unpaired electrons trapped by the oxygen defects in the lattice.[37] Electron paramagnetic resonance (EPR) shows a significant difference between the two systems. That further reveals that Ile-α-MnO$_2$ has a higher concentration of oxygen defects than that of α-MnO$_2$, agreeing with the XPS analysis. The N$_2$ adsorption-

desorption measurement indicates that the specific surface area of Ile-α-MnO$_2$ is 105.2 m^2/g, which is much higher than α-MnO$_2$ (41.4 m^2/g) (Figure S8). The curve also shows H3 hysteresis loops, reflecting their mesoporous structure. The abundant mesopores can provide pathways to facilitate ion transport in electrochemical reactions, thereby improving the specific capacity and rate capability.[38]

Scanning electron microscopy (SEM) images were conducted to investigate the morphological evolution of Mn-based cathodes, as shown in Figure 2d-e and Figure S9. All the Ile-α-MnO$_2$ display well-defined nanorod structures, while the α-MnO$_2$ samples present rod agglomeration in addition to the rod structure to form a blocky structure with a non-uniform morphology. The uniform nanorod morphology of Ile-α-MnO$_2$ might owe to the presence of Ile that promotes the stable organic-inorganic hybridized interface formation on α-MnO$_2$ surface with covalent Mn-N bonds and inhibits MnO$_2$ agglomeration. The microstructures of pristine α-MnO$_2$ and Ile-α-MnO$_2$ were further investigated by transmission electron microscopy (TEM). The typical diameter of a nanorod could be around 30 nm (Figure S10a), with the high crystallinity feature as shown from the high-resolution TEM (HRTEM) image (Figure 2f). The HRTEM clearly illustrates that there are uniform Ile layers coated on α-MnO$_2$ with a thickness of approximately 3 nm. α-MnO$_2$ presents a typical nanorod-like structure with a diameter of about 50 nm (Figure S11 a and b). The lattice fringes show a planar spacing of ~0.7 nm (Figure S10 b and c), corresponding to the d-spacing of the (110) crystal plane of the I4/m space group in α-MnO$_2$. From the HRTEM image of α-MnO$_2$ (Figure S11c), the distances between the lattice fringes were measured to be 0.5 nm, corresponding to the (200) crystallographic planes of α-MnO$_2$.[39] Moreover, the elemental mapping image in Figure 2g illustrates the presence of Mn, O, K and N elements in Ile-α-MnO$_2$ nanorods with uniform spatial distribution. Whereas, there are only Mn, O and K elements identified in the pristine α-MnO$_2$ (Figure S11d).

The electrochemical performance of Ile-α-MnO$_2$ was carefully evaluated in working batteries by cyclic voltammetry (CV), galvanostatic charge and discharge (GCD), galvanostatic

intermittent titration technique (GITT), and electrochemical impedance spectroscopy (EIS) tests as shown in Figure 3. A series of AZIBs were assembled using α-MnO$_2$ and Ile-α-MnO$_2$ electrodes as cathodes, Zn metal foil as anode, and 2 M ZnSO$_4$ aqueous solution with 0.2 M MnSO$_4$ additive as electrolyte. Figure 3a shows the similar CV curves identified in α-MnO$_2$ and Ile-α-MnO$_2$ at a scan rate of 0.2 mV/s and a voltage window of 0.8-1.8 V. The CV curves present two cathodic peaks at around 1.2 and 1.3 V and two anodic peaks at 1.5 and 1.6 V (vs. Zn^{2+}/Zn), corresponding to the insertion/extraction of Zn^{2+} ions and protons, respectively.[40] The smaller electrode polarization with narrower voltage gaps was observed from Ile-α-MnO$_2$ (0.22 V, 0.29 V) than that of the pristine α-MnO$_2$ (0.25 V, 0.33 V). Also, a more pronounced redox strength and smaller potential hysteresis were identified in the Ile-α-MnO$_2$ relative to the pristine α-MnO$_2$. This suggests that the Ile coating can enhance the electrochemical reaction activity and accelerate the electrode kinetics.[41] The ten CV curves for Ile-α-MnO$_2$ almost overlap with each other except for the first circle, indicating that the electrochemical cycling is highly reversible (Figure S12). The GCD also verifies a two-step charge/discharge process with an obvious voltage plateau, consistent with the CV tests (Figure S13). Notably, the Ile-α-MnO$_2$ exhibits a superior specific capacity of 334.9 mAh/g at a low current density of 0.1 A/g, surpassing the specific capacity of the pristine α-MnO$_2$ (307.8 mAh/g). It is also higher than most of the reported cathode materials in AZIBs in the literature (Figure 3b), and their electrochemical features are summarized in Table S2. To further understand the superior performance of Ile-α-MnO$_2$, the GCD curves of the pristine α-MnO$_2$ were conducted under identical conditions with Ile-α-MnO$_2$ at current densities ranging from 0.1 to 1.0 A/g (Figure 3c and Figure S14). It is worth noting that the discharge plateau of the Ile-α-MnO$_2$ electrode is significantly higher than that of the pristine α-MnO$_2$ (1.34 V vs. 1.30 V). The charge/discharge curves are clearly distinguishable from the characteristic platforms, even at a high current density of 1.0 A/g. Those results indicate that Ile-α-MnO$_2$ achieves higher activities and faster reaction kinetics than the pristine α-MnO$_2$ cathode.

Ile-α-MnO$_2$ electrode also exhibits the higher reversible capacity than α-MnO$_2$ at different current densities from 0.1 to 1.0 A/g, as shown in Figure 3d, verifying its higher rate performance and greater capacity retention. Specifically, the reversible capacities of the Ile-α-MnO$_2$ electrode were 334.8, 295.4, 266.7, 228.8, 194.5 and 167.1 mAh/g with current densities increasing from 0.1 to 0.2, 0.3, 0.5, 0.8, and 1.0 A/g, respectively. It demonstrates the excellent rate performance of Ile-α-MnO$_2$. The output capacity of the Ile-α-MnO$_2$ cathode can recover to 325.1 mAh/g when the current density is further reduced back to 0.1 A/g, showcasing its remarkable reversibility. The high-rate capability of Ile-α-MnO$_2$ can be attributed to the organic-inorganic hybridization achieved through interface engineering, resulting in an increased specific surface area with abundant diffusion channels and a high number of active sites. The generation of oxygen defects also enhances the electronic conductivity of Ile-α-MnO$_2$ indicated by the smaller band gap (1.06 eV) than that (1.29 eV) of the pristine α-MnO$_2$ from DFT calculations (Figure S15). Furthermore, the strong Mn-N bonds can stabilize the surface coating on the α-MnO$_2$ surface and suppress interfacial side reactions as well as enhancing energy storage reversibility. As expected, Ile-α-MnO$_2$ exhibits outstanding long-term cycling stability even at a high current density of 1.0 A/g with a reversible capacity of 153.8 mAh/g after 2000 cycles and a capacity retention of 85%. In contrast, the α-MnO$_2$ electrode presents only 95.6 mAh/g capacity after 200 cycles and capacity retention as low as 65% (Figure 3e). Those strongly demonstrate the pivotal role of the coated Ile on the structural stability of the α-MnO$_2$ cathode. The Ragone plots summarize the specific energy and power densities of the Ile-α-MnO$_2$ (Figure 3f). The device can achieve a high energy density of 448.8 Wh/kg at 134.8 W/kg and can maintain 233.1 Wh/kg at 1294.5 W/kg, which are higher than recently reported AZIBs (Table S3).
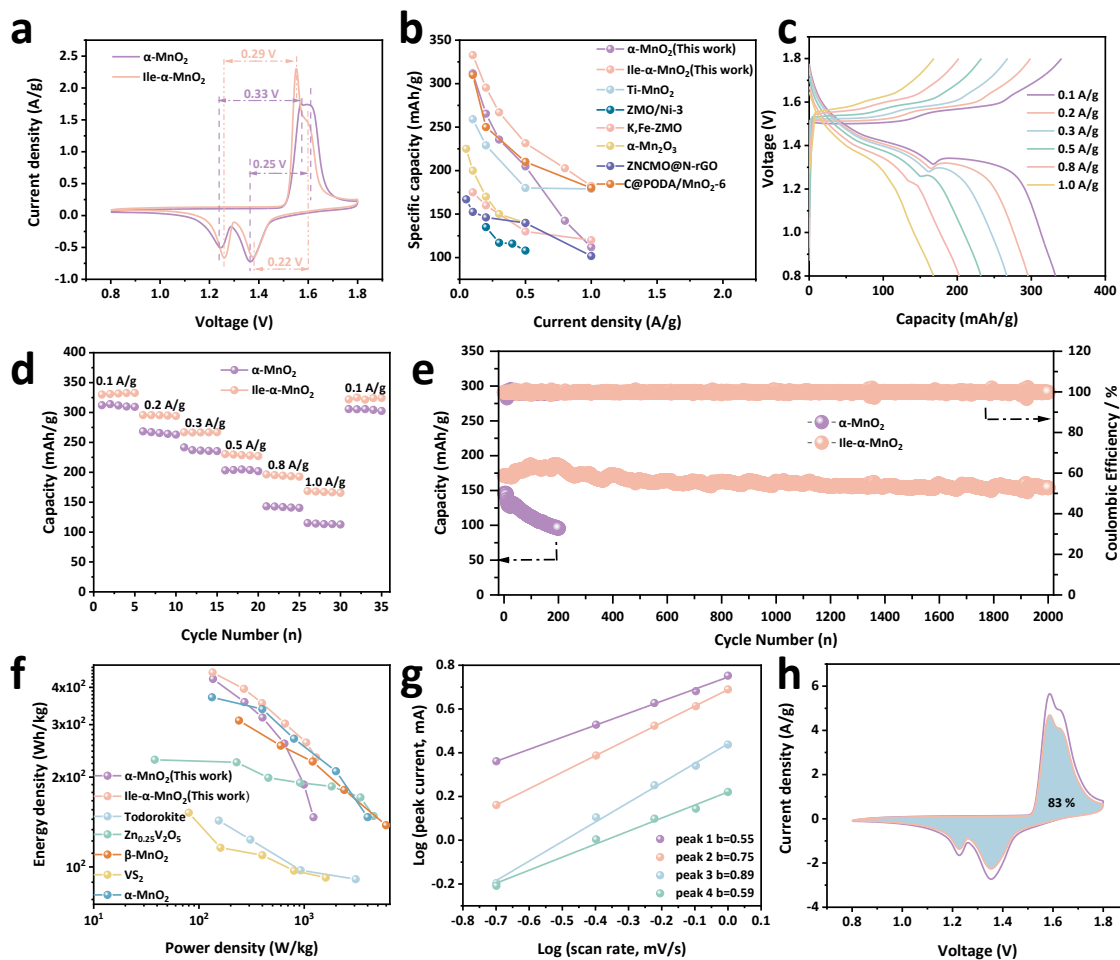
Figure 3. The electrochemical performance of Ile-α-MnO₂ and α-MnO₂. (a) CV curves of Ile-α-MnO₂ and α-MnO₂ at a scan rate of 0.2 mV/s. (b) Comparison of rate performance. (c) GCD curves of Ile-α-MnO₂ at different current densities from 0.1 to 1.0 A/g. (d) Rate performance at different specific currents for the two electrode materials. (e) Long-term cycling performance and Coulombic efficiency of Ile-α-MnO₂ and α-MnO₂ at 1.0 A/g. (f) Comparison of Regone plot. (g) The corresponding plots of log (peak current) *vs.* log (scan rate) at each peak. (h) Capacitive contributions to the total current in Ile-α-MnO₂ at 1 mV/s.

To further understand the electrochemical kinetics of both Ile-α-MnO₂ and α-MnO₂ electrodes, CV measurements were performed at different scan rates from 0.2 to 1.0 mV/s. Figure S16 shows the CV curves of Ile-α-MnO₂ at different scan rates. Two reduction peaks and two oxidation peaks were identified in each curve, which are consistent with the charging/discharging plots. Unlike typical ion diffusion behavior, the square root of the peak current (i) is not well proportional to the scan rate (v), indicating a combination of non-Faraday and Faraday behaviors in the charge/discharge process. On the basis of a previous study,[42] the

correlation equation between i and v is as follows:

$$i = av^b \tag{2}$$

which can be rephrased as

$$\log(i) = b\log(v) + \log(a) \tag{3}$$

where a and b are adjustable parameters. When the value of b is 0.5, ion diffusion dominates the charge/discharge process. Figure 3g illustrates the $\log(i)$ vs. $\log(v)$ plots of the four reduction and oxidation peaks. The b values of peaks 1, 2, 3, and 4 are 0.55, 0.75, 0.89, and 0.59, respectively. It indicates that both the diffusion and the capacitive processes contribute to electrochemical performance. This leads to rapid Zn^{2+} insertion/extraction and long-lasting cyclic stability. Similarly, the kinetic analysis was also carried out for α-MnO$_2$ system (Figure S17 a and b). All the CV curves display four distinct redox peaks, and the b values are all between 0.5 and 1. This also indicates the synergistic effect of diffusion-controlled Faraday process and capacitance-controlled behavior on the electrochemical kinetics of α-MnO$_2$ cathode. The proportion of the Zn^{2+} capacitance effect can be further quantified by dividing the current response i at a fixed potential V into a capacitance effect and a diffusion control response ($k_2v^{1/2}$). The capacitive effect can be calculated via the following equation:[43]

$$i = k_1v + k_2v^{1/2} \tag{4}$$

that can be portrayed as

$$i/v^{1/2} = k_1v^{1/2} + k_2 \tag{5}$$

For the same scan rate, the diffusion contribution is higher in Ile-α-MnO$_2$ compared to the α-MnO$_2$ (Figures 3h and S17c). The capacitance contributions reach 71%, 75%, 78%, 79% and 83% with scan rate increasing (Ile-α-MnO$_2$, Figure S18), and also are higher than those of α-MnO$_2$ at different scan rates (Figure S17d). This is due to the formation of organic-inorganic interface, which increases the number of surface and the contact sites for Zn^{2+} ions. Meanwhile, the presence of anionic defects facilitates the entry of charge carriers into the interior of electrode, enabling rapid ion embedding and dislodging, thereby increasing its diffusion

14

capacitance.[44] With a larger diffusion pseudocapacitance, Zn^{2+} ions are more prone to rapid insertion/extraction behaviour, allowing them to easily penetrate the material's interior. This promotes rapid self-diffusion of Zn^{2+} in the Ile-α-MnO_2 structure, leading to an increase in capacity. To sum up, at different scan rates, the diffusion pseudocapacitance of Ile-α-MnO_2 is higher than that of α-MnO_2. The Ile surface coating facilitates easy access for charge carriers into the material's interior and enables fast insertion/extraction behavior, thereby enhancing diffusion control capacity.
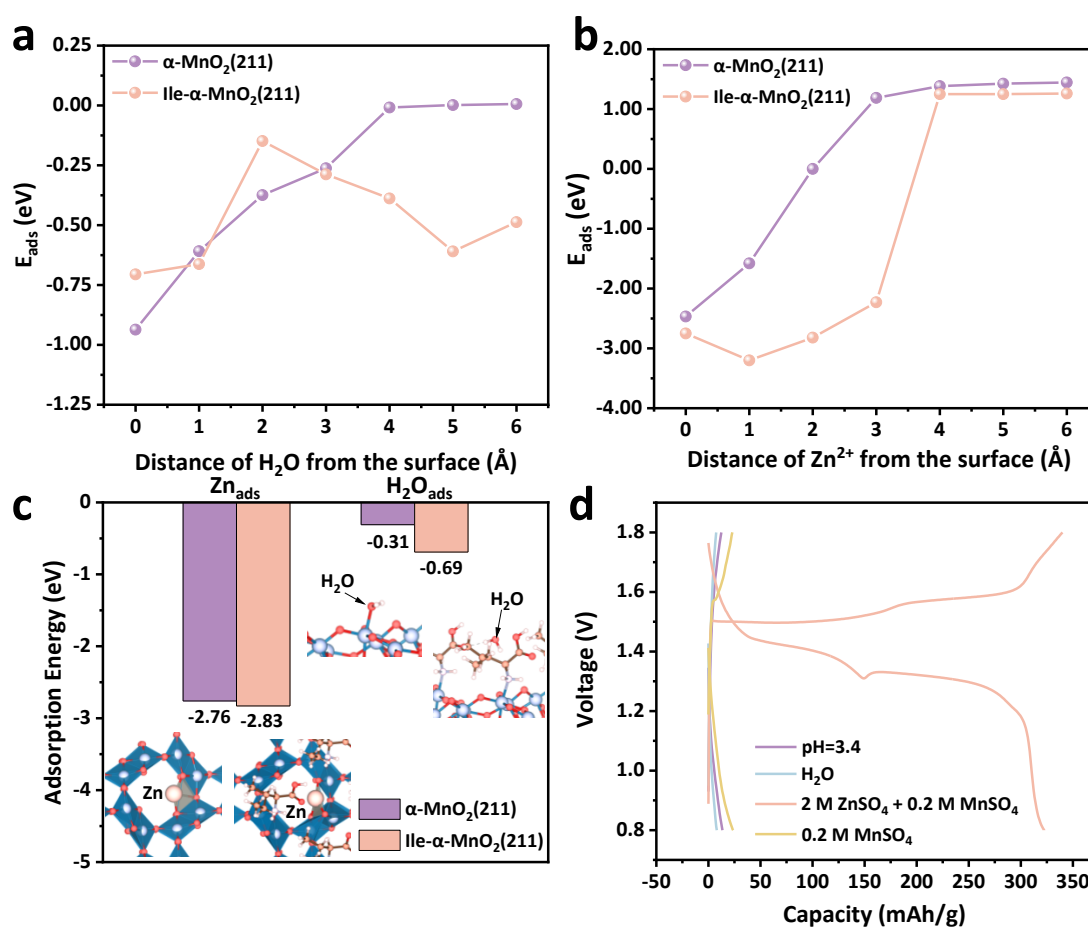
Figure 4. Adsorption and energy storage mechanism. (a)~(b) are Zn^{2+} and H_2O adsorption energy changes from the gas-phase to the surface of α-MnO_2(211). (c) The adsorption of Zn^{2+} and H_2O at α-MnO_2(211) and Ile-α-MnO_2(211) systems, respectively. (d) The GCD curves of Ile-α-MnO_2 in different electrolytes.

It is the stage to understand the structure stability and, energy storage mechanism as well as ion migration behavior. H_2O solvent was considered one of the culprits in the corrosion of

MnO$_2$ electrode. DFT calculations were conducted to address the protection of Ile coating layer on α-MnO$_2$ with mitigating water corrosion but allowing Zn^{2+} diffusion. Precisely, Zn^{2+} and H$_2$O adsorption behaviours were investigated. Zn^{2+} was found to adsorb in the cavity of both pristine α-MnO$_2$(211) and Ile-α-MnO$_2$(211) systems. The adsorption energy (E$_{ads}$) of Zn^{2+} are -2.83 eV in pristine α-MnO$_2$(211) and -2.76 eV in Ile-α-MnO$_2$(211), respectively. It indicates the Ile coating layer would not affect Zn^{2+} intercalation into α-MnO$_2$. However, the adsorption of H$_2$O is completely different. The E$_{ads}$ is -0.69 eV at the Mn site on the pristine α-MnO$_2$(211) surface, while it reduces to only -0.31 eV on the Ile-α-MnO$_2$(211). This is due to the coating of Ile on the α-MnO$_2$(211) surface that covers the active Mn sites, resulting in only weak physical interactions between H$_2$O and the system. The adsorption energy changes of those two species from the gas-phase to the surface of α-MnO$_2$(211) along Z direction were then explored. From Figure 4a, it can be observed that the E$_{ads}$ shows a downward trend for both the pristine α-MnO$_2$(211) and the Ile-α-MnO$_2$(211) system, suggesting that there are no barriers for Zn^{2+} adsorption on either system. Interestingly, the presence of Ile coating layer promotes Zn^{2+} adsorption and intercalation into α-MnO$_2$(211), verifying the attraction of Ile molecules towards Zn^{2+}. In terms of H$_2$O adsorption, without the Ile coating layer modification, the E$_{ads}$ of H$_2$O strengthens progressively from the gas phase to α-MnO$_2$(211) surface. However, it is noteworthy that there exists at least 0.46 eV energy barrier that H$_2$O has to overcome when it approaches the α-MnO$_2$(211) surface in the presence of Ile coating layer, preventing H$_2$O accessing the electrode surface. As a consequence, the Ile molecular layer coated on the α-MnO$_2$ effectively attracts and facilitates Zn^{2+} penetration through the coating layer while impeding H$_2$O infiltration into the α-MnO$_2$(211) surface, leading to the mitigation of side reactions and corrosion of α-MnO$_2$ cathode. The GCD curves were tested in different electrolytes, which show great agreement with our DFT results (Figure 4d). At a current density of 0.1 A/g, Ile-α-MnO$_2$ contributed a specific capacity of 322.4 mAh/g in a 2 M ZnSO$_4$ + 0.2 M MnSO$_4$ (pH=3.4) electrolyte. However, in deionized water and sulfuric acid solution with

the same pH, the specific capacities of α-MnO$_2$ electrode become only 8 and 13.5 mAh/g, respectively. The capacity of α-MnO$_2$ with 0.2 M MnSO$_4$ electrolyte is also only 23.7 mAh/g. Therefore, the encapsulation of the Ile coating layer can inhibit water and sulfate ions entering the material while promoting the rapid adsorption and intercalation of zinc ions, hindering the side reactions of the α-MnO$_2$ cathode. It is known that Mn-based electrodes are susceptible to Mn dissolution in the electrolyte during the charging and discharging process. Excessive dissolution of Mn leads to the collapse of electrode, resulting in poor cycling and rapid capacity decay. Hence, the post-cycling inductively coupled plasma mass spectrometry (ICP-MS) tests were performed in 2 M ZnSO$_4$ (Table S4) to further elucidate the dissolution of manganese in the electrolyte. After 50 cycles, the content of Mn in electrolyte Ile-α-MnO$_2$ is 24.5 μg/L, which is lower than that in pristine α-MnO$_2$ (92.4 μg/L). The reduction of Mn dissolution in Ile-α-MnO$_2$ is attributed to the hybridization interface that stabilizes the Mn sites of Ile-α-MnO$_2$ and inhibits the dissolution, thereby enhancing cycling stability performance.

Ex-situ XRD at different cutoff voltages were collected to reveal changes in chemical composition and electronic structure during the redox process. Figures 5a and 5b demonstrate the ex-situ XRD patterns at different voltage states, which can also reflect the zinc storage mechanism in Ile-α-MnO$_2$. As can be observed from the localized enlargements of the ex-situ XRD 5-25°, 30-80°, new diffraction peaks at 9.5°, 15.4°, 21.2°, 32.7°, 34.2°, and 58.4° (Figure 5c), which are attributed to the characteristic peaks of ZHS (Zn$_4$(OH)$_4$SO$_6$·3H$_2$O (JCPDS No. 39-0689), Zn$_4$(OH)$_4$SO$_6$·0.5H$_2$O (JCPDS No. 44-0673)) and ZnMn$_2$O$_4$ (JCPDS No. 39-0689), respectively. These new phases were continuously formed during discharging and gradually disappeared during charging. The intercalation of protons in the cathode generates OH$^-$ anions that accumulate near the electrode surface and further react with Zn^{2+} and SO$_4^{2-}$ to produce ZHS.[45,46] During the discharged/charged process, ZnMn$_2$O$_4$ formation is because of Zn^{2+} inserting into the Ile-α-MnO$_2$. The repeated formation and dissolution of ZHS and ZnMn$_2$O$_4$ as evidenced by their repeated diffraction peaks confirm the excellent reversibility of the

electrochemical co-insertion process of Zn^{2+} and protons. Subsequently, ex-situ XPS spectra of the pristine Ile-α-MnO$_2$ and in fully charged and discharged states were tested to further demonstrate the reaction mechanism of co-embedding. The O 1s XPS spectra of the fully charged, discharged, and the pristine states imply that Ile-α-MnO$_2$ significantly promotes the reversible proton insertion (Figure 5d). In the fully discharged state, the reversible O-H signal increases and maintains high proton insertion kinetics.[47] Figure 5e shows the high-resolution Zn 2p XPS spectra of Ile-α-MnO$_2$ at different states of charge. In the pristine state, the Zn 2p XPS spectrum exhibits the absence of zinc ions. Upon discharging to -0.8 V, strong Zn 2p signals were detected, while the intensity significantly decreased after charging to 1.8 V. It evidences mainly the intercalation of Zn^{2+} in the cathode material during charging and discharging. Additionally, the oxidation-state change of Mn under charging and discharging was evaluated using the spin energy splitting (ΔE) of the Mn 3s bistate peak (Figure 5f). A previous study indicates that the increasing binding energies of Mn-based cathode materials in AZIBs are related to the decrease in the oxidation state of Mn.[48] After complete discharge, the ΔE value of Mn 3s increases by 4.1 eV compared to that in the fully charged state (3.5 eV), indicating that the valence state of Mn decreases to +2 after co-insertion of H^+ and Zn^{2+}. Whereas, with the extraction of ions and protons, the oxidation state of Mn gradually recovered. The Fourier transform infrared spectroscopy (FTIR) spectra also indicate that the Ile-α-MnO$_2$ has a more pronounced reactivity and better reversibility. When the battery was discharged, the content of Zn-basic sulfate gradually increased, while the Zn-basic sulfate gradually disappeared during charging (Figure S19). That implies the reversible reaction between the cathode and H^+ in this process. Meanwhile, the generation and disappearance of Zn-O bonds during the charging and discharging process are also evidence of the reversible reaction of Zn ion intercalation. It is also demonstrated that Ile-α-MnO$_2$ has good cyclic reversibility.

Furthermore, the morphologies of Ile-α-MnO$_2$ and α-MnO$_2$ electrodes before and after cycling were explored (Figure S20). Both samples gradually change from the initial long

nanorods to the flower-like nanosheets after cycling. Precisely, the long nanorod structures gradually transformed to nanosheets and generate more disordered structures. The original long-range ordered structures transform into many short ring structures and form more porous structures. During the cycling process, the electrolyte gradually penetrated and the nanorod structure changed, showing good wettability.[49,50] Unlike the original α-MnO$_2$, there are more uniform and consistent nanosheets formed after cycling of Ile-α-MnO$_2$. The XRD curves after cycles were tested for Ile-α-MnO$_2$ and α-MnO$_2$, as shown in Figure S21. Compared to α-MnO$_2$, the diffraction peaks at 18.2°, 33.1°, 36.4° and 38.9° (ZnMn$_2$O$_4$, JCPDS No. 39-0689) after cycling are significantly more intense for Ile-α-MnO$_2$. It is further verified that the Ile coating facilitates the accumulation of Zn^{2+} from the electrolyte to the α-MnO$_2$ cathode.

To explore the difference in electrochemical kinetics between Ile-α-MnO$_2$ and α-MnO$_2$, both electrochemical impedance spectroscopy (EIS) and GITT tests were conducted.[51] The EIS results reveal that the R$_{ct}$ value of Ile-α-MnO$_2$ is 6.3 Ω, significantly lower than that (11.8 Ω) of the pristine α-MnO$_2$, suggesting that Ile-α-MnO$_2$ cathode has enhanced charge-transfer capability (Figure 5g). This was also verified by the GITT tests in Figures 5h and 5i. The D$_{Zn}{}^{2+}$ values of Ile-α-MnO$_2$ were calculated to be 2.3×10^{-11} and 1.2×10^{-14} cm^2/s, respectively. Those are much higher than those of α-MnO$_2$ (2.3×10^{-12} -1.1×10^{-16} cm^2/s), indicating Ile-α-MnO$_2$ facilitates Zn^{2+} diffusion and achieves better rate performance than α-MnO$_2$.
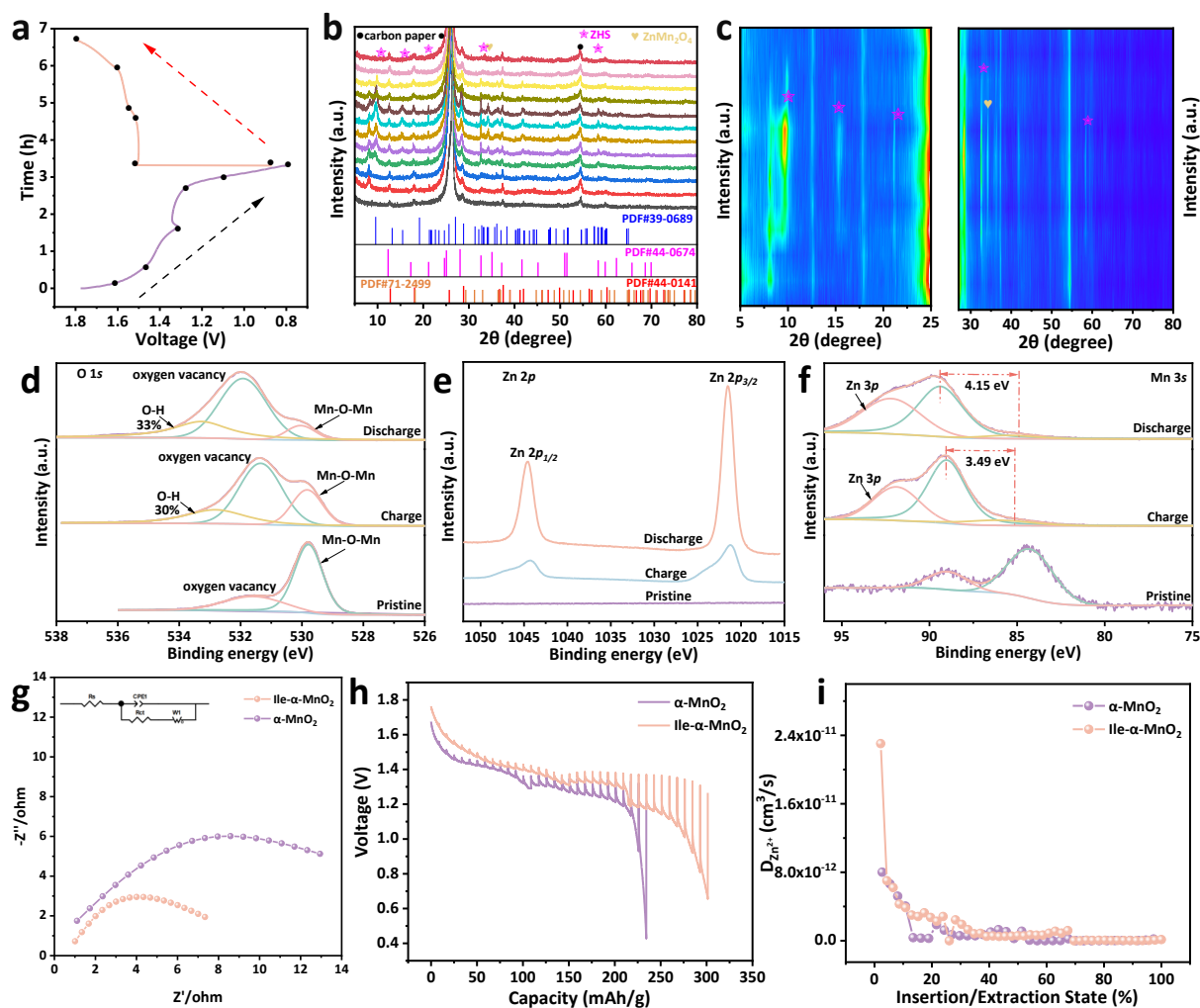
Figure 5. Energy storage mechanism analysis. (a) GCD curves with marked voltage states for ex-situ characterization. (b) Ex-situ analyses of XRD patterns at the selected points in Ile-α-MnO$_2$. (c) Local magnification of ex-situ XRD at different voltages. (d)~(f) are the Mn 2p, Zn 2p and Mn 3s XPS spectra of Ile-α-MnO$_2$ in pristine, discharged and charged states. (g) Nyquist plots of the Ile-α-MnO$_2$ and α-MnO$_2$. (h) The GITT profiles of the Ile-α-MnO$_2$ and α-MnO$_2$: GITT curves of discharge. (i) Corresponding Zn^{2+} diffusion coefficient in the discharge process.

3. Conclusion

In summary, we proposed an organic-inorganic composite interface engineering using the Ile coating layer to enhance the cycling stability of α-MnO$_2$ cathode material from theoretical perspective. Experimental characterization confirms the well-defined morphology of Ile-α-MnO$_2$ via the stable Mn-N bonds reinforcing the interface structures. The compact and stable interface can inhibit the dissolution of Mn and enhance the cycling stability of the material. Ile

coating allows for three-dimensional diffusion of Zn^{2+}, thereby improving ion transport kinetics. Furthermore, the oxygen vacancies formed during electrochemical oxidation not only improve the electronic conductivity but also provide more active sites for Zn^{2+} storage. Consequently, the prepared Ile-α-MnO$_2$ exhibits fast Zn^{2+} and proton co-embedding as well as good reversibility. The Ile-α-MnO$_2$ electrode finally contributed a very high specific capacity of 334.8 mAh/g at 0.1 A/g and the fabricated device achieved a high energy density of 448.8 Wh/kg at 134.8 W/kg. This study presents a simple method using low-cost raw materials to fabricate a Mn-based cathode, achieving high structural stability and superior performance characteristics.

Declaration of Competing Interest

The authors declare that they have no known competing financial interests or personal relationships that could have appeared to influence the work reported in this paper.

Data Availability Statement

The data that support the findings of this study are available from the corresponding author upon reasonable request.

References

[1] L. Ma, N. Li, C. Long, B. Dong, D. Fang, Z. Liu, Y. Zhao, X. Li, J. Fan, S. Chen, S. Zhang and C. Zhi, *Adv. Funct. Mater.* 2019, 29, 1906142.

[2] K. Zhu, S. Wei, H. Shou, F. Shen, S. Chen, P. Zhang, C. Wang, Y. Cao, X. Guo, M. Luo, H. Zhang, B. Ye, X. Wu, L. He and L. Song, *Nat. Commun.* 2021, 12, 6878.

[3] Y. Lv, Y. Xiao, L. Ma, C. Zhi, S. Chen, *Adv. Mater.* 2022, 34, e2106409

[4] J. Yang, R. Zhao, Y. Wang, Z. Hu, Y. Wang, A. Zhang, C. Wu, Y. Bai, *Adv. Funct. Mater.* 2023, 33, 2213510.

[5] J. Yue, S. Li, S. Chen, J. Yang, X. Lu, Y. Li, R. Zhao, C. Wu, Y. Bai, *Energy Mater Adv.* 2023, 4, 0050.

[6] N. Zhang, X. Chen, M. Yu, Z. Niu, F. Cheng, J. Chen, *Chem. Soc. Rev.* 2020, 49, 4203-4219.

[7] Y. Yuan, R. Sharpe, K. He, C. Li, M. T. Saray, T. Liu, W. Yao, M. Cheng, H. Jin, S. Wang, K. Amine, R. Shahbazian-Yassar, M. S. Islam, J. Lu, *Nat. Sustainability* 2022, 5, 890.

[8] H. Pan, Y. Shao, P. Yan, Y. Cheng, K. S. Han, Z. Nie, C. Wang, J. Yang, X. Li, P. Bhattacharya, K. T. Mueller, J. Liu, *Nat. Energy* 2016, 1, 16039

[9] Y. Luo, Y. Bai, A. Mistry, Y. Zhang, D. Zhao, S. Sarkar, J. V. Handy, S. Rezaei, A. C. Chuang, L. Carrillo, K. Wiaderek, M. Pharr, K. Xie, P. P. Mukherjee, B. X. Xu and S. Banerjee, *Nat. Mater.* 2022, 21, 217-227.

[10] S. Islam, M. H. Alfaruqi, V. Mathew, J. Song, S. Kim, S. Kim, J. Jo, J. P. Baboo, D. T. Pham, D. Y. Putro, Y.-K. Sun and J. Kim, *J. Mater. Chem. A* 2017, 5, 23299-23309.

[11] S. Jia, L. Li, Y. Shi, C. Wang, M. Cao, Y. Ji, D. Zhang, *Nanoscale* 2024, 16, 1539.

[12] H. Li, H. Yao, X. Sun, C. Sheng, W. Zhao, J. Wu, S. Chu, Z. Liu, S. Guo, H. Zhou, *Chem. Eng. J.* 2022, 446, 137205.

[13] H. Yang, W. Zhou, D. Chen, J. Liu, Z. Yuan, M. Lu, L. Shen, V. Shulga, W. Han, D. Chao, *Energy Environ. Sci.* 2022, 15, 1106.

[14] J. Kim, D. Kim, D. Oh, H. Lee, J. Lee, Y. Jung, *J. Power Sources* 2015, 274, 1254.

[15] J. Lu, C. Zhan, T. Wu, J. Wen, Y. Lei, A. J. Kropf, H. Wu, D. Miller, J. Elam, Y. Sun, *Nat. Commun.* 2014, 5, 5693.

[16] X. Yao, Y. Zhao, F. Castro, L. Mai, *ACS Energy Lett.* 2019, 4, 771.

[17] Q. Zhao, A. Song, S. Ding, R. Qin, Y. Cui, S. Li, F. Pan, *Adv. Mater.* 2020, 32, 2002450.

[18] P. Xiong, B. Sun, N. Sakai, R. Ma, T. Sasaki, S. Wang, J. Zhang, G. Wang, *Adv. Mater.* 2020, 32, 1902654.

[19] Y. Tan, Z. Chen, Z. Tao, A. Wang, S. Lai, Y. Yang, *Angew. Chem. Int. Ed.* 2023, 62, e202217744.

[20] E. Pomerantseva, Y. Gogotsi, *Nat. Energy* 2017, 2, 17089.

[21] Y. Xia, Z. Hong, L. Zhou, S. Chen, Z. Luo, S. Jin, Y. Huang, Y. Jiang, Y. Wu, *J. Energy Chem.* 2023, 87, 153.

[22] Q. Wen, H. Fu, Z. Wang, Y. Huang, Z. He, C. Yan, J. Mao, K. Dai, X. Zhang, J. Zheng, *J. Mater. Chem. A* 2022, 10, 17501.

[23] B. Wang, R. Zheng, W. Yang, C. Hou, Q. Zhang, K. Li, Y. Li, H. Wang, *ACS Appl. Energy Mater.* 2023, 6, 12249.

[24] Z. Luo, Y. Xia, S. Chen, X. Wu, R. Zeng, X. Zhang, H. Pan, M. Yan, T. Shi, K. Tao, B. B. Xu, Y. Jiang, *Nano-Micro Lett.* 2023, 15, 205.

[25] X. Feng, M. Li, J. Yin, T. Cui, F. Li, Y. Cheng, S. Ding, X. Xu, J. Wang, *ACS Appl. Mater. Interfaces* 2024, 16, 12544.

[26] J. Jia, P. Zhang, L. Chen, *Catal. Sci. Technol.* 2016, 6, 5841.

[27] P. Zhao, G. Li, H. Zheng, S. Lu, P. Peng, *Sci. Rep.* 2021, 11, 4751.

[28] Y. Ding, S. Zhang, J. Li, Y. Sun, B. Yin, H. Li, Y. Ma, Z. Wang, H. Ge, D. Su, T. Ma, *Adv. Funct. Mater.* 2023, 33, 2210519.

[29] Y. Dong, J. Sun, Y. Shen, Z. Wang, W. Wang, Z. Song, X. Zhao, Y. Mao, *Chem. Eng. J.* 2023, 473, 145130.

[30] H. Chi, P. Zhang, J. Xiong, Y. Wei, Y. Li, Z. Zhao, J. Liu, J. Jiao, *Appl. Surf. Sci.* 2023, 608, 155116.

[31] X. Liu, K. Zhou, L. Wang, B. Wang, Y. Li, *J. Am. Chem. Soc.* 2009, 131, 3140-3141.

[32] C. He, Y. Wang, Z. Li, Y. Huang, Y. Liao, D. Xia, S. Lee, *Environ. Sci. Technol.* 2020, 54, 12771.

[33] C. Zuo, F. Chao, M. Li, Y. Dai, J. Wang, F. Xiong, Y. Jiang, Q. An, *Adv. Energy Mater.* 2023, 13, 2301014.

[34] Y. Zhao, S. Zhang, Y. Zhang, J. Liang, L. Ren, H. J. Fan, W. Liu, X. Sun, *Energy Environ. Sci.* 2024, 17, 1279.

[35] C. Zhang, Q. Chen, X. Ai, X. Li, Q. Xie, Y. Cheng, H. Kong, W. Xu, L. Wang, M.- S. Wang, H. Yang, D.-L. Peng, *J. Mater. Chem. A* 2020, 8, 16323-16331.

[36] J. Li, S. Zhang, Y. Ding, Y. Sun, J. Yang, H. Li, T. Ma, B. Yin, *Chem. Commun.* 2023, 59, 4316.

[37] Y. Ding, S. Zhang, M. Bat-Erdene, J. Li, Y. Sun, M. Li, M. Liu, H. Li, Y. Zhang, H. Ge, G. Zhao, Z. Yu, B. Yin, T. Ma, *Energy Stor. Mater.* 2023, 63, 103010.

[38] M. Li, Y. Ding, S. Zhang, Y. Sun, M. Liu, J. Zhao, B. Yin, T. Ma, *Small Structures* 2024, 5, 2300371.

[39] N. Jabeen, Q. Xia, S. V. Savilov, S. M. Aldoshin, Y. Yu, H. Xia, *ACS Appl. Mater. Interfaces* 2016, 8, 33732.

[40] J. Huang, Z. Wang, M. Hou, X. Dong, Y. Liu, Y. Wang, Y. Xia, *Nat. Commun.* 2018, 9, 2906.

[41] X. Chen, W. Li, Z. Zeng, D. Reed, X. Li, X. Liu, *Chem. Eng. J.* 2021, 405, 126969

[42] K. Zhang, M. Park, L. Zhou, G. H. Lee, W. Li, Y. M. Kang, J. Chen, *Adv. Funct. Mater.* 2016, 26, 6728.

[43] D. Chao, C. Zhu, P. Yang, X. Xia, J. Liu, J. Wang, X. Fan, S. V. Savilov, J. Lin, H. J. Fan, Z. X. Shen, *Nat. Commun.* 2016, 7, 12122.

[44] T. Brezesinski, J. Wang, S.H. Tolbert, B. Dunn, *Nat. Mater.* 2010, 9, 146.

[45] Y. Zhao, P. Zhang, J. Liang, X. Xia, L. Ren, L. Song, W. Liu, X. Sun, *Energy Stor. Mater.* 2022, 47, 424-433.

[46] D. Wang, S. Zhang, C. Li, X. Chen, W. Zhang, X. Ge, H. Lin, Z. Shi and S. Feng, *Small*, 2022, 18, e2105970.

[47] A. Zhang, X. Wang, R. Zhao, Y. Wang, J. Yue, J. Yang, C. Wu, Y. Bai, *Angew. Chem. Int. Ed.* 2023, e202313163.

[48] Y. Deng, H. Wang, M. Fan, B. Zhan, L.-J. Zuo, C. Chen, L. Yan, *J. Am. Chem. Soc.* 2023, 145, 20109.

[49] Y. Mai, D. Zhang, Y. Qiao, C. Gu, X. Wang, J. Tu, *J. Power Sources* 2012, 216, 201-207.

[50] T. Wang, S. Zhang, X. Yan, M. Lyu, L. Wang, J. Bell, H. Wang, *ACS Appl. Mater. Interfaces* 2017, 9, 15510-15524.

[51] X. Zhu, Z. Cao, X. L. Li, L. Pei, J. Jones, Y. N. Zhou, P. Dong, L. Wang, M. Ye, J. Shen, *Energy Storage Mater.* 2022, 45, 568.